Northumbria University
NEWCASTLE

University**Library**

Impaired Condensin Complex and Aurora B kinase underlie mitotic and chromosomal defects in hyperdiploid B-cell ALL

Oscar Molina[1,2*], Meritxell Vinyoles[1], Isabel Granada[2,3], Heleia Roca-Ho[1,2], Francisco Gutierrez-Agüera[1,2], Luis Valledor[4], Carlos M López-López[4], Pablo Rodríguez-González[4], Juan L Trincado[1], Sofía T Menéndez[2,5], Deepali Pal[6,7], Paola Ballerini[8], Monique den Boer[9], Isabel Plensa[10], M. Mar Perez-Iribarne[10], Sandra Rodríguez-Perales[11], Maria-Jose Calasanz[12], Manuel Ramírez-Orellana[13], René Rodríguez[2,5], Mireia Camós[10,14,15], Maria Calvo[16], Clara Bueno[1,2], Pablo Menéndez[1,2,17*]

[1]Josep Carreras Leukemia Research Institute and Department of Biomedicine, School of Medicine. University of Barcelona. Barcelona. Spain.
[2]Centro de Investigación Biomédica en Red de Cáncer (CIBER-ONC), ISCIII, Spain.
[3]Hematology Laboratory, Germans Trias i Pujol University Hospital-Catalan Institute of Oncology, Badalona, Spain.
[4]Department of Physical and Analytical Chemistry, University of Oviedo, Asturias, Spain.
[5]Instituto de Investigación Sanitaria del Principado de Asturias (ISPA), Hospital Universitario Central de Asturias, Oviedo, Spain.
[6]Wolfson Childhood Cancer Research Centre, Northern Institute for Cancer Research, Newcastle University, Newcastle upon Tyne, UK.
[7]Department of Applied Sciences, Northumbria University. Newcastle upon Tyne, UK.
[8]Pediatric Hematology, A. Trousseau Hospital, Paris. France.
[9]Princess Máxima Center for Pediatric Oncology, Utrecht, The Netherlands.
[10]Hematology Laboratory. Institut Recerca Hospital Sant Joan de Déu, Barcelona. Spain.
[11]Molecular Cytogenetics Group, Centro Nacional de Investigaciones Oncológicas. Madrid, Spain.
[12]CIMA Lab Diagnostics, Universidad de Navarra, Pamplona, Spain.
[13]Hematology Diagnostic Laboratory. Hospital Niño Jesús, Madrid. Spain.
[14]Leukemia and other pediatric hemopathies. Developmental Tumors Biology Group. Institut de Recerca Hospital Sant Joan de Déu Barcelona, Barcelona, Spain.
[15]Centro de Investigación Biomédica en Red de Enfermedades Raras (CIBERER), ISCIII, Barcelona. Spain.
[16]Scientific and Technological Centers, Universitat de Barcelona (CCiTUP) Campus Clínic, Barcelona, Spain.
[17]Institució Catalana de Recerca i Estudis Avançats (ICREA). Barcelona. Spain.

Short Title: AURKB and condensin defects in hyperdiploid B-ALL.

Text word count: 4210 words.
Abstract word count: 206 words
Scientific category: Lymphoid neoplasia

*Correspondence should be addressed to:
Oscar Molina PhD or Pablo Menendez PhD
Josep Carreras Leukemia Research Institute
School of Medicine. University of Barcelona. Casanova 143, 08036. Barcelona. Spain.
omolina@carrerasresearch.org ; pmenendez@carrerasresearch.org

KEY POINTS:

- HyperD-ALL shows a delay in early mitosis at prometaphase associated to defects in chromosome alignment and segregation.
- Impaired condensin complex leads to defective AURKB, triggering chromatid cohesion defects and mitotic slippage of HyperD-ALL blasts.

ABSTRACT

B-cell acute lymphoblastic leukemia (B-ALL) is the most common pediatric cancer, and high-hyperdiploidy (HyperD) identifies the most common subtype of pediatric B-ALL. Despite HyperD is an initiating oncogenic event affiliated to childhood B-ALL, the mitotic and chromosomal defects associated to HyperD B-ALL (HyperD-ALL) remain poorly characterized. Here, we have used 54 primary pediatric B-ALL samples to characterize the cellular-molecular mechanisms underlying the mitotic/chromosome defects predicated to be early pathogenic contributors in HyperD-ALL. We report that HyperD-ALL blasts are low proliferative and show a delay in early mitosis at prometaphase, associated to chromosome alignment defects at the metaphase plate leading to robust chromosome segregation defects and non-modal karyotypes. Mechanistically, biochemical, functional and mass-spectrometry assays revealed that condensin complex is impaired in HyperD-ALL cells, leading to chromosome hypocondensation, loss of centromere stiffness and mis-localization of the chromosome passenger complex proteins Aurora B Kinase (AURKB) and Survivin in early mitosis. HyperD-ALL cells show chromatid cohesion defects and impaired spindle assembly checkpoint (SAC) thus undergoing mitotic slippage due to defective AURKB and impaired SAC activity, downstream of condensin complex defects. Chromosome structure/condensation defects and hyperdiploidy were reproduced in healthy CD34+ stem/progenitor cells upon inhibition of AURKB and/or SAC. Collectively, hyperdiploid B-ALL is associated to defective condensin complex, AURKB and SAC.

INTRODUCTION

B-cell acute lymphoblastic leukemia (B-ALL) is characterized by the accumulation of abnormal immature B-cell precursors (BCP) in the bone marrow (BM), and is the most common pediatric cancer[1]. B-ALL is a heterogeneous disease with distinct biological-prognostic subgroups classified according to the stage at which BCPs are stalled in differentiation and cytogenetic/molecular markers[1]. Importantly, different biological subtypes of B-ALL have distinct causal mechanisms and show different clinical outcomes[1-3].

High hyperdiploid B-ALL (HyperD-ALL) is the most common subtype of childhood B-ALL and is characterized by the presence of 51-67 chromosomes in leukemic cells[4-7]. HyperD-ALL comprises ~30% of pediatric B-ALL and usually has a favourable clinical outcome[5,8,9]. Of note, the distribution of chromosome gains is not random and preferentially show gains of chromosomes X, 4, 6, 10, 14, 17, 18 and 21[5,10]. Hyperdiploidy is an initiating oncogenic event in B-ALL and secondary alterations necessary for clinical B-ALL accumulate subclonally and postnatally[5,7,11,12]. Despite hyperdiploidy is the most common B-ALL in children, very little is known about its etiology and pathogenesis, and many questions about the biology of HyperD-ALL remain unanswered. Despite its favourable clinical outcome, a precise knowledge of the physiopathogenic mechanisms underlying HyperD-ALL is necessary because in absolute numbers, the morbidity/mortality associated to HyperD-ALL still represent a clinical challenge.

HyperD-ALL is proposed to arise in a BCP *in utero*[7]. However, the causal molecular mechanisms of hyperdiploidy in BCPs remain elusive. In this sense, faithful chromosome segregation is essential for maintaining the genomic integrity of eukaryotic cells, and deficient chromosome segregation leads to aneuploidy and cancer[13-15]. Three main and non-mutually exclusive mechanisms, interconnected with mitosis[16], underlie chromosome missegregation: (i) defects in

bipolar spindle formation, (ii) defects in chromosome structure and function, and (iii) defects in the spindle assembly checkpoint (SAC) which controls proper mitosis until chromosomes are properly attached to the spindle[14-16]. Indeed, SAC defects have been proposed to be an underlying pathogenic mechanism in rare cases of ETV6/RUNX1+ B-ALL with near-tetraploid karyotypes[17]. Therefore, abnormal mitotic control in BCP could be at the origin of hyperdiploidy in B-ALL.

Here, we used a large cohort of primary pediatric B-ALL samples (n=54) to gain insights into the cellular and molecular mechanisms underlying mitotic/chromosome defects predicated to be at the origin of pediatric HyperD-ALL. Our data reveal that HyperD-ALL blasts show robust condensin complex defects and defective Aurora B kinase (AURKB) activity leading to abnormal mitotic progression and chromosome missegregation. Functional inhibition of AURKB and the SAC in normal hematopoietic stem/progenitor cells (HSPCs) reproduced hyperdiploid karyotypes with abnormal chromosome structure. We conclude that defects in condensin complex, AURKB, and SAC are associated to HyperD-ALL, likely representing a pathogenic mechanism.

METHODS

Pediatric B-ALL leukemic samples and cell lines

Diagnostic BM samples from B-ALL pediatric patients were obtained from collaborating hospitals. B-ALL diagnosis was based on FAB and WHO classifications[1]. **Table S1** summarizes main clinico-biological data of the patients. Fetal tissue was collected from developing embryos aborted at 18 to 22 weeks of pregnancy, obtained from the MRC/Wellcome Trust Human Developmental Biology Resource upon informed consent and approval by our local ethics committee. The B-ALL cell lines SEM, REH and MHH-CALL-2 (DMSZ, Germany) were used for confirmatory studies. This study was approved by our Institutional Review Ethics Board (Barcelona Clínic-Hospital, HCB/2014/0687), and patient samples were accessed upon informed consent.

In vivo expansion of B-ALL blasts

All experimental procedures were approved by the Animal Care Committee of the Barcelona Biomedical Research Park (DAAM7393). Primary blasts ($5x10^5$) were expanded *in vivo* in sublethally irradiated 8-to-14-week-old non-obese diabetic/LtSz-scid IL-$2Ry^{-/-}$ mice (NSG) upon intra-BM transplantation[18]. PB was monitored by FACS for leukemia engraftment. Primografts were sacrificed when engraftment reached 10-15% in PB, typically representing >80% engraftment in BM. Blasts were isolated from BM and spleen by density-gradient centrifugation for downstream analysis. For FACS analysis of leukemic engraftment, PBMCs were stained with anti-human HLA-ABC-FITC, CD19-PE and CD45-APC antibodies (BD-Biosciences), and analysed using a FACS Canto-II cytometer.

Indirect immunofluorescence

B-ALL cells were spun on poly-L-lysine-coated coverslips (500g, 3min) before fixation. Cells were fixed and permeabilized with Triton X100-containing buffer (5min). Cells were blocked with permeabilization-buffer containing 1-3%BSA (1hour, 37°C), and incubated overnight at 4°C with

primary antibodies (**Table S2**). Cells were washed with permeabilization-buffer, and incubated (45min) with fluorophore-conjugated secondary antibodies (Jackson Labs). All antibodies were diluted in blocking-buffer. Slides were mounted with Vectashield-DAPI (VectorLab). Details of chromosome spreading for immunofluorescence are provided in **Supplementary Methods**.

Confocal microscopy and image acquisition

Microscope images were captured using a fully-equipped Zeiss LSM880 laser-scanning spectral confocal microscope equipped with an AxioObserver Z1 inverted microscope. DAPI, Alexa-488, Alexa Fluor-555 and Alexa Fluor-647 images were acquired sequentially using 405, 488, 561 and 633 lasers, dichroic beam splitters, emission detection ranges of 415-480nm, 500-550nm, 571-625nm and 643-680nm, respectively, and the confocal pinhole was set at 1 Airy units (AU). An acoustic optical beam splitter was used at the same emission detection ranges. Spectral detection was performed using two photomultipliers and one central GaAsP detector used for the acquisition of Alexa-647. Images were acquired in a 1024x300pixels format, zoom was set at 2, pixel size at 53x53nm and dwell time at 0.51µsec. Z-stacks were acquired at a 300nm step size to reconstruct the entire nuclei volume. Immunofluorescence signal quantification was performed using FIJI-ImageJ (NIH). Details of image quantifications are provided in **Supplementary Methods**.

Details for i*n vitro* culture/expansion of B-ALL cells and HSPCs, chromosome function and cytogenetic analysis, fluorescence quantification, western-blot and protein analysis, mass-spectometry (MS) assays, cell cycle and phosphor-H3S10 quantification, RT-PCR, chromatin immunoprecipitation and RNA-sequencing are provided in **Supplementary Methods** and **Tables S3** and **S4**.

185 **Statistical analysis**

186 Statistical comparisons were performed using Graphpad Prism. Mean values and their standard
187 error of the mean (s.e.m) were calculated for each variable. All data was analyzed according to
188 the test indicated in the appropriate figure legends on the indicated number of experiments. Non-
189 HyperD were compared with HyperD B-ALLs. $P<0.05$ was considered statistically significant.

190

191

RESULTS

HyperD-ALL cells are low proliferative and show a delay in early mitosis

Aneuploid cells typically display a gene signature characterized by an up-regulation of genes involved in oxidative stress response, membrane functions and immune response regulation coupled to a down-regulation of genes involved in cell proliferation and nucleic acid metabolism[19-21]. We first analysed the transcriptomic signature of HyperD-ALL blasts using a RNA-Seq dataset from HyperD-ALL patients (n=58) and non-HyperD B-ALL patients (n=30, non-aneuploid, **Suppl methods**)[22]. A Gene Ontology analysis of the 26,239 genes differentially expressed between primary HyperD-ALL and non-HyperD B-ALLs confirmed an aneuploidy-like gene expression signature characterized by the up-regulation of pathways associated with oxidative stress, protein turn-over, cell death, immune system activation and membrane functions (**Fig 1a,b**), and down-regulation of pathways associated to nucleic acid metabolism and tRNA biology (**Fig 1a**,**c**). Consistent with this, we found that the aneuploid pediatric B-ALL cell line CALL-2 (doubled-up hypodiploid karyotype: 51XX,+X,+18,+der(18)t(15;18),+21,+21)[23] exhibits a significantly lower proliferative rate than the non-HyperD-ALL cell lines SEM and REH (**Fig 1d**). Mechanistically, CALL-2 cells revealed a 5-fold increase in apoptosis coupled to an accumulation in G2/M (**Fig 1e,f**), indicating cell division/mitotic defects in aneuploid B-ALL cells.

To further characterize the mitotic progression of HyperD-ALL cells, we stained CALL-2, SEM and REH for DAPI, tubulin, pericentrin and the anti-centromere antibody (ACA) to unequivocally identify the different mitotic phases[24] (**Fig 1g**). Consistent with the FACS data, immunofluorescence (IF) analysis revealed that CALL-2 cells accumulated in early mitosis, specifically at prometaphase/metaphase, with a concomitant delay in late mitosis (**Fig 1h,i**).

Chromosome alignment defects in prometaphase underlie the mitotic delay of HyperD-ALL primary blasts

Cancer cell lines do not phenocopy faithfully the molecular complexity of the disease. Furthermore, despite CALL-2 is the only childhood HyperD-ALL cell line available, it actually represents a doubled-up hypodiploid B-ALL cell line[23]. We thus aimed to analyse the proliferation/mitotic defects in childhood HyperD-ALL primary blasts. Because leukemic primary cells fail to expand *ex vivo*[25-27], we co-cultured B-ALL blasts with nestin+ fetal BM (FBM)-derived MSCs which support short-term proliferation of primary B-ALL blasts without compromising clonal composition[28] (**Fig 2a, Fig S1a,b**). Similar to cell lines, non-HyperD-ALL primary cells grown on Nestin+ FBM-MSCs expanded 5-fold over a 6-day period while HyperD-ALL primary blasts failed to expand at all *ex vivo* (**Fig 2b**). FACS analysis using BM diagnostic samples also showed an increase in both apoptosis and frequency of G2/M cells in primary HyperD-ALL cells (**Fig 2c,d**). To further link proliferative impairment with mitotic defects, we analysed the mitotic progression in dividing B-ALL primary blasts expanded *in vivo* in NSG mice (**Fig 2e, S2a**). Xenografted blasts were processed and IF-stained for the DNA-Kinetochore-Spindle staining to unambiguously identify each mitotic phase (**Fig 2f**). Consistent with cell lines, HyperD-ALL primary blasts accumulated in early mitosis, at prometaphase/metaphase, with a concomitant delay in late mitosis (telophase and cytokinesis; **Fig 2g, Fig S2b**).

Because chromosomes align at the metaphase plate in the prometaphase-to-metaphase transition, we then inspected dividing cells in early mitosis to distinguish between prometaphase (non-aligned chromosomes) and metaphase (aligned chromosomes) cells. We observed a robust decrease of HyperD-ALL blasts with aligned metaphase plates (**Fig 2h**), confirming chromosome alignment defects in early mitosis in HyperD-ALL cells. Chromosome alignment relies on the dynamics of chromosome biorentation to the spindle poles[29]. We thus analysed the dynamics of chromosome biorientation in primary B-ALL blasts by generating monopolar spindles and prometaphase arrest with monastrol (a spindle bipolarity inhibitor), followed by treatment with the

proteasome inhibitor MG132 which further arrests dividing cells in metaphase[30] (**Fig 2i**). Strikingly, non-HyperD-ALL primary blasts properly aligned chromosomes at the metaphase plate in ~90% of the metaphases (**Fig 2j,k**). However, HyperD-ALL samples showed a massive decrease in the number of cells with aligned chromosomes at the metaphase plate (~45%) (**Fig 2j,k**). Noteworthy, the defective chromosome biorientation in HyperD-ALL cells were confirmed in B-ALL cell lines (**Fig S3a**). Thus, the impaired proliferation of HyperD-ALL blasts may result from mitotic defects in prometaphase-metaphase due to aberrant chromosome alignment at the metaphase plate.

Chromosome misalignment defects results in chromosome missegregation and non-modal karyotypes in HyperD-ALL blasts

Because defects in chromosome alignment often result in chromosome missegregation[24], we next analysed the rates of chromosome segregation defects, mainly lagging chromosomes and anaphase bridges, in B-ALL blasts (**Fig 3a**). To overcome the accumulation of HyperD-ALL cells in early mitosis, B-ALL primary blasts were treated with the cytokinesis inhibitor Blebbistatin[31]. We found that HyperD-ALL primary blasts displayed a significant ~4-fold higher number of late mitosis with chromosome segregation defects (**Fig 3b**).

Since chromosome missegregation leads to aneuploidy, we analysed the modal karyotype distribution in 12 diagnostic B-ALL samples. We found a high chromosome stability in non-HyperD B-ALL samples, with a modal chromosome number of 46 in >80% of the metaphases analysed (**Fig 3c**,**d**, **Fig S4**). However, HyperD-ALL blasts showed an increased karyotype instability defined by the presence of a major clone (40% of the cells) and minor clones with non-modal chromosome distributions (**Fig 3c, d**, **Fig S4**). These results were confirmed by FISH analysis for chromosomes 12 and 21 (**Fig 3e, f**). Chromosome instability in HyperD-ALL cells was

268 further confirmed in B-ALL cell lines (**Fig S3b,c**). Collectively, chromosome alignment defects
269 result in chromosome segregation defects and subsequent non-modal karyotypes in HyperD-ALL
270 blasts.
271
272 **HyperD-ALL blasts show chromosome hypocondensation and loss of centromere**
273 **stiffness due to condensin complex defects**
274 We next investigated the mechanisms leading to these mitotic/chromosome defects. IF analysis
275 of the spindle using the DNA-Kinetochore-Spindle staining showed similarly low frequency of
276 mitotic blasts with spindle abnormalities such as multipolar or disorganized spindles in non-
277 HyperD- and HyperD-ALL (**Fig 4a**). Moreover, defects in bipolar spindle formation frequently lead
278 to cytokinesis defects and tetraploidization[32]. Since no (near)-tetraploid cells were observed in
279 any HyperD-ALL patient (**Fig 3c,d**, **Fig S4**), we ruled out defects in spindle formation in HyperD-
280 ALL blasts.
281
282 We next assessed whether chromosome structure and function underlies the mitotic defects
283 observed in HyperD-ALL. We first examined the chromosome morphology of Carnoy-fixed
284 pediatric B-ALL blasts (**Table S1**). While non-HyperD-ALL metaphases mostly showed normal
285 rod-shaped chromosomes, ~60% of HyperD-ALL metaphases displayed curly-
286 shaped/hypocondensed chromosomes with irregular borders (**Fig 4b, S5a**). Importantly,
287 intrapatient comparison of diploid normal hematopoietic cells *versus* hyperD blasts confirmed that
288 chromosome hypocondensation specifically occurs in HyperD-ALL cells (10% vs 70%, **Fig S5b**).
289 Chromosome hypocondensation defects were further confirmed in B-ALL cell lines (**Fig S5c**). We
290 next scored formaldehyde-fixed B-ALL samples for chromosome structure/condensation, and
291 found significantly more metaphases containing hypocondensed and unstructured fuzzier and

292 wider chromosomes in HyperD-ALL than in non-HyperD-ALL blasts (80% vs 20%,p<0.001, **Fig**
293 **4c,d, S5d**), excluding an impact of the fixative on chromosome structure/condensation defects.
294
295 Condensin complexes are major components of the chromosome scaffold that regulate
296 chromosome compaction and higher-order chromatin organization during mitosis[33-36]. The
297 chromosome structure/condensation defects observed in HyperD-ALLs, prompted us to analyse
298 in chromosome spreads from primary B-ALL samples the binding pattern of SMC2, a major
299 component of condensin complexes. Non-HyperD-ALL blasts showed a normal beaded pattern
300 for SMC2, spreading along the chromatids with a centromere enrichment (**Fig 4e**). In contrast,
301 SMC2 was hardly detectable in neither chromatids nor centromeres, and showed an abnormal
302 staining pattern in HyperD-ALL blasts (**Fig 4e**). Indeed, 3D image quantification of SMC2 staining
303 revealed a significantly lower volume of SMC2 in chromosomes from HyperD-ALL blasts (**Fig 4f**,
304 **Fig S5e**).
305
306 To further characterize the defects in condensin complexes in HyperD-ALL samples, we analysed
307 by WB in PDX-expanded B-ALL cells, the distinct protein members specific for each of the two
308 human condensin complexes (complex I and II), which play a differential contribution to mitotic
309 chromosome organization/segregation (**Fig 4g**). Protein analysis confirmed the lower levels of
310 SMC2 in HyperD-ALL blasts, and revealed that both condensin complexes (CAPD2 and CAPD3)
311 were similarly affected (**Fig 4h,i**). Strikingly, however, no differences were observed at the RNA
312 level for any of the condensin complex members between HyperD-ALL and non-HyperD-ALL
313 samples (**Fig S5f**), suggesting that post-translational modifications (PTM) may underlie
314 condensin complex defects in HyperD-ALL blasts.
315

316 Compelling data strongly suggest that PTMs are essential for regulating condensin loading to
317 chromosomes[37,38]. We thus performed MS analyses for both SMC2 acetylation and CAPD2
318 phosphorylation levels after immunoprecipitation of the condensin complexes with anti-SMC2
319 (**Fig S5g**), and found increased levels of both SMC2 acetylation and CAPD2 phosphorylation in
320 HyperD-ALL samples (**Fig 4j-l**), suggesting that PTMs regulating condensin activation may
321 represent a mechanism underlying condensin defects in HyperD-ALL blasts.
322
323 Condensin complexes set the stiffness of the centromeric chromatin required for withstand the
324 spindle pulling forces during metaphase[29], and SMC2 depletion results in increased
325 intercentromeric distances in metaphase chromosomes[39,40]. To analyse centromere stiffness in
326 HyperD-ALL blasts, we measured the intercentromeric distances between sister-kinetochore
327 pairs in metaphase-arrested blasts (**Fig 4m**). For this, B-ALL blasts were metaphase-arrested
328 with chromosomes under tension (non-relaxed length) or without tension (rest length) from the
329 spindle, by using either the proteasome inhibitor MG132 or the microtubule depolymeriser
330 colcemid, respectively. HyperD-ALL blasts consistently displayed a significant longer
331 intercentromeric distance than non-HyperD-ALL blasts (**Fig 4n,o**). Collectively, PTMs of
332 condensin members may induce a defective condensin complex which leads to high-order
333 chromosome organization defects and impaired centromere stiffness/stretching at metaphase in
334 HyperD-ALL blasts.
335
336 **Kinetochores are normal in HyperD-ALL blasts**
337 The kinetochore binds microtubules at centromeres and regulates chromosome segregation[41].
338 CENP-A (centromere-specific histone H3) and NDC80/NUF-2 are key centromere chromatin
339 markers of the inner and outer kinetochore plate, respectively, which control kinetochore's
340 assembly. CENP-A overlaps with the condensin complex and it is flanked by the heterochromatin

histone marks H3K9me3 and H3K27me3[42-47]. We thus prompted to study whether the condensin defects observed in HyperD-ALL blasts are associated to centromeric chromatin defects and destabilization of the kinetochore. ChIP-qPCR assays showed no differences of CENP-A, H3K9me3 or H3K27me3 levels at centromeres of HyperD-ALL blasts as compared to non-HyperD-ALL blasts (**Fig S6a**). Moreover, quantitative confocal microscopy analysis revealed very similar levels of NUF-2 between HyperD-ALL and non-HyperD-ALL blasts (**Fig S6b,c**), indicating that despite impaired centromere stiffness, the centrochromatin is not epigenetically impaired and the kinetochore forms normally in HyperD-ALL blasts.

The chromosome passenger complex (CPC) proteins AURKB and Survivin are mis-localized from the inner-centromere in early mitotic HyperD-ALL blasts

We next aimed to analyse the cellular mechanisms by which the impaired condensin complex leads to mitotic/chromosome defects in HyperD-ALL blasts. We first analysed the CPC, a protein complex composed by AURKB and the accessory subunits Survivin, Borealin and INCENP. The CPC regulates the SAC to ensure proper kinetochore-microtubule attachment, and was shown mis-localized from the inner-centromere in cells with defective condensin complex[34,48,49]. Prometaphase-arrested nonHyperD-ALL primary blasts revealed a normal chromosomal distribution of both AURKB and Survivin mainly concentrated in the inner-centromere (**Fig 5a,b**). However, HyperD-ALL blasts showed an aberrant chromosomal distribution of both AURKB and Survivin, diffusely distributed throughout the chromosome arms rather than concentrated in the inner-centromere (**Fig 5a,b**). Quantification of both AURKB and Survivin at the inner-centromeres confirmed a significant decrease of both CPC proteins in centromeres of HyperD-ALL blasts (**Fig 5c,d, S7a,b**). To further characterize the localization of AURKB and Survivin, we analysed the frequency of chromosomes showing either centromeric or scattered localization (**Fig 5e**), and confirmed that HyperD-ALL blasts preferentially showed scattered localization throughout the

chromosome arms (**Fig 5f,g**). These results were reproduced using B-ALL cell lines (**Fig S7c,d**). Of note, the overall chromosome-wide expression levels of both AURKB and phospho-histone H3 at Serine 10 (H3S10p), the major readout of AURKB activity, were significantly reduced in HyperD-ALL blasts (**Fig 5h,i**). Finally, we generated condensin complex I-defective non-HyperD-ALL cell lines by knocking down CAPD2, and confirmed the mis-localization of AURKB from the inner-centromere (**Fig S7e,f**). Taken together, mis-localization of the CPC proteins AURKB and Survivin in early mitosis represents a major mechanism linking defective condensin complex and chromosome alignment/segregation defects in HyperD-ALL blasts.

Defective AURKB is associated with loss of chromatid cohesion and SAC impairment in HyperD-ALL blasts

The confined localization of AURKB at the inner-centromere is essential for chromatid cohesion and proper SAC activity[30,50,51]. Indeed, analysis of chromosome spreads revealed that 75% of the metaphases from HyperD-ALL blasts displayed “rail-road chromosomes”, a common phenotype reflecting premature chromatid separation (PCS) due to reduced chromatid cohesion at centromeres (**Fig 5j, S8a**). These results were reproduced using B-ALL cell lines (**Fig S8b**).

AURKB controls chromosome biorientation/alignment at the metaphase plate through phosphorylation of different SAC proteins[30,50,52,53]. We thus reasoned that AURKB defects may underlie the progression towards late mitosis of HyperD-ALL blasts with mis-aligned chromosomes by preventing SAC activation. To test this, we co-cultured B-ALL primografts on Nestin+ FBM-MSC in the presence of nocodazol, which generates persistently unattached kinetochores leading to SAC activation and mitotic accumulation (**Fig 5k**), and found that nocodazol-treated HyperD-ALL blasts did not accumulate in mitosis as efficiently as non-HyperD-ALL blasts (**Fig 5l,m**). These results were reproduced in B-ALL cell lines (**Fig S8c**). Cell cycle

391 analysis further confirmed that HyperD-ALL blasts do not arrest in G2/M after nocodazol
392 treatment but they accumulate in G0/G1 (**Fig 5n,o**), strongly suggesting mitotic slippage.
393 Apoptosis was not different between HyperD-ALL and non-HyperD-ALL blasts (**Fig S8d**).
394 Noteworthy, the metaphase-to-anaphase promoting regulator MAD2L2, whose loss leads to
395 accelerated mitosis and mitotic aberrations[54] was found downregulated in HyperD-ALL blasts (**Fig**
396 **5p**). Collectively, HyperD-ALL cells show chromatid cohesion defects and undergo mitotic
397 slippage most likely due to defective AURKB and impaired SAC activity, downstream of
398 condensin complex defects.
399
400 **Inhibition of AURKB and SAC in CD34+ HSPCs reproduces chromosome structure defects**
401 **and hyperdiploid karyotypes**
402 We next prompted to functionally model whether defective AURKB and impaired SAC activity
403 could reproduce the phenotype observed in HyperD-ALL primary blasts. Because hyperD-ALL
404 was shown to have a prenatal origin and pre-leukemic hyperdiploid precursors are found at
405 birth[55,56], we exposed fetal BM-derived CD34+ HSPCs to the AURKB inhibitor ZM447439 and/or
406 to the SAC inhibitor Reversine for 48h, and then processed cells for cytogenetics analysis (**Fig**
407 **6a,b**). Both AURKB and SAC inhibition in CD34+ HSPCs reproduced chromosome structure
408 defects observed in HyperD-ALL (**Fig 6b, S9a**). They both drastically increased (compared to
409 controls) the frequency of CD34+ HSPCs with micronuclei, a *bona fide* marker of chromosome
410 instability (**Fig 6c**), hypocondensed chromosomes (**Fig 6d**), and metaphases with PCS reflecting
411 loss of chromatid cohesion (**Fig 6e**).Such chromosome structure defects were maintained and/or
412 slighted potentiated when both AURKB and SAC were simultaneously inhibited (**Fig 6b-e**). Of
413 note, despite we could not reliably assess the karyotypes of reversine-treated CD34+ HSPCs due
414 to massive chromosome damage, AURKB inhibition resulted in ~30% of the CD34+ HSPCs
415 displaying hyperdiploid karyotypes (**Fig 6f, S9b,c**). In addition, cell cycle analysis revealed

massive alterations in DNA ploidy, confirming genomic imbalances in CD34+ cells upon treatment with AURKB or SAC inhibitors (**Fig 6g**). The chromosome structure defects and hyperdiploid karyotypes reproduced in CD34+ cells reinforce defective AURKB and SAC as an underlying cellular/molecular mechanism in hyperdiploidy B-ALL.

DISCUSSION

This is the most comprehensive study to date on the cellular mechanisms underlying the mitotic and chromosome defects contributing to the pathophysiology of pediatric HyperD-ALL. Here, we have developed robust *in vitro* assays using nestin+ fetal BM-MSCs and *in vivo* PDX to successfully expand primary B-ALL leukemic samples. Such *ex vivo* and *in vivo* expansion of B-ALL leukemic samples provided enough mitotic/dividing primary blasts for addressing many biological questions in a large cohort of 54 primary B-ALL samples, thus highlighting the clinical relevance of our work. The only available hyperD-ALL cell line CALL-2 was used throughout the study for confirmatory and gain-of-function studies, and consistently phenocopied the data generated using primary HyperD-ALL primary cells. This cell line originates from a doubled-up hypodiploid B-ALL[23], suggesting that the same mitotic/chromosomal defects here reported may underlie the pathogenesis of hypo-diploid B-ALL patients. Future studies, however, should be done in HypoD-ALL patients who are rare but clinically dismal.

We demonstrate that in contrast to nonHyperD-ALL, HyperD-ALL blasts show reduced proliferative rates coupled to a delay in early mitosis at prometaphase. Such a delay in early mitosis is associated to chromosome alignment defects at the metaphase plate which, in fact, lead to chromosome segregation defects and non-modal karyotypes. Despite karyotype heterogeneity, HyperD-ALL primary blasts show a major clone that most likely represents the fittest clone after cell adaptation to aneuploidy[57]. These data supports previous studies showing the presence of cytogenetically different subclones in HyperD-ALL[58-61].

Mechanistically, HyperD-ALL primary blasts and cell lines did not show abnormalities in bipolar spindle and kinetochore formation. However, they displayed important chromosome structure and function defects, a major mechanism regulating chromosome segregation which is essential for maintaining the genomic integrity of cells[13-15]. HyperD-ALL cells showed robust defects in several

members of the condensin complexes including SMC2 (levels reduced at chromosome scaffolds), CAPD2 and CAPD3. Biochemical, functional and MS assays revealed that PTMs of condensin complex proteins may represent a mechanism underlying defective condensin complexes in HyperD-ALL cells. Of note, no mutations were found in condensin complex- encoding genes in HyperD-ALL patients, ruling out genomic mutations as the cause of the defective condensin complex in HyperD-ALL patients.

Consequently, high-order chromosome architecture defects are notorious, and include chromosome hypocondensation and loss of centromere rigidity revealed by increased intercentromeric distances. Consistently, a recent study has reported chromosome architecture defects and lower expression of CTCF in HyperD-ALL samples[62]. Furthermore, AURKB, the catalytic subunit of the CPC, and Survivin are mis-localized from the inner-centromere in early mitosis, further linking defective condensin with chromosome segregation defects in HyperD-ALL blasts. According to the essential localization of AURKB at the inner-centromere to protect chromatid cohesion and for proper SAC activity[30,50,51], HyperD blasts show chromatid cohesion defects as observed by PCS and impaired SAC, leading to mitotic slippage. Impaired SAC activity explains why HyperD-ALL blasts proceed to late mitosis with misaligned chromosomes at the metaphase plate, thus leading to chromosome segregation defects. Importantly, chromosome hypocondensation and hyperdiploidy were functionally reproduced in CD34+ HSPC upon inhibition of AURKB and/or SAC, reinforcing defective condensin complex, AURKB and SAC as underlying cellular and molecular mechanisms in HyperD-ALL (**Figure 7**). Although they are likely instrumental in the pathophysiology of the HyperD-ALL, whether these findings are causal or consequential to hyperdiploidy remains an open question under investigation.

This is the first cellular and molecular in-depth characterization of the mitotic and chromosomal defects of HyperD-ALL using a cohort of 54 B-ALL primary samples. It represents a highly relevant study because B-ALL is the most common pediatric cancer. Studies in monozygotic twins with concordant HyperD-ALL and retrospective analysis of HyperD clones in cord blood indicated that HyperD clones arise prenatally[7], and that hyperdiploidy is an initiating oncogenic event generating a preleukemic clone which then requires secondary mutations to trigger a full-blown leukemia[63]. Therefore, a better mechanistic understanding of how hyperdiploidy occurs and how secondary alterations are acquired becomes crucial not only to propose novel therapeutic targets but also to prevent the progression/relapse of HyperD-ALL. These defects in condensin complex-AURBK-SAC axis open up new avenues for modelling HyperD-ALL by genetically engineering of HSPCs, which will be crucial to further address the causal contribution of these defects to the origin of HyperD in B-ALL.

From a diagnostic-clinical standpoint, the high-order chromatin/chromosome structural defects observed in HyperD-ALL explains very well the difficulties that clinical cytogeneticists have historically encountered to obtain metaphases of standard quality from these patients, thus challenging the cytogenetic diagnostic[3]. In addition, despite the favourable clinical outcome of HyperD-ALL, unravelling the physiopathogenic mechanisms underlying HyperD-ALL is necessary because in absolute numbers, the morbidity/mortality associated to HyperD-ALL still represent a clinical challenge. In sum, this study seeds light on the mechanisms underlying the mitotic and chromosome defects involved in the pathogenesis of HyperD-ALL and offers molecular targets (Condensin complex members, CPC members -AURKB- or the SAC) for potential pharmacological intervention in the most frequent molecular subtype of pediatric acute leukemia.

AUTHOR CONTRIBUTIONS

OM conceived the study, designed and performed experiments, analyzed and interpreted the data, and wrote the manuscript. CB designed and performed experiments, analyzed and interpreted the data. MV,LV,CML-L,PR-G,IG,HRH,FGA,JLT,ST,DP,RR and MaC performed experiments and analyzed data. PB,MdB,IP,MMPI,SRP,MJC,MRO, and MiC provided patient's samples and data. PM conceived the study, designed experiments, interpreted the data, and wrote the manuscript.

ACKNOWLEDGMENTS

We would like to dedicate this paper to the memory of our collaborator Anna Bosch (CCiTUB, Barcelona) and to our patients. We were particularly inspired by AMC. We would like to thank Dr. Dolors Costa (Hospital Clínic, Barcelona), Elisenda Coll (CCiTUB, Barcelona), Drs. Samanta Zanneti, Talía Velasco, Raúl Torres and Belén López-Millán (PM laboratory) for technical input, Dr. Ana Losada (CNIO, Madrid) for providing condensin Ab, Dr. M. Alba Abad and Prof. William C Earnshaw (University of Edinburgh) for critical discussions, and Prof Anthony Moorman (University of Newcastle) and Anindita Roy (Oxford University) for providing whole genome and RNA sequencing data, respectively. We thank to "Biobanc de l'Hospital Infantil Sant Joan de Déu per la Investigació", integrated in the Spanish Biobank Network of ISCIII for the sample and data procurement. We thank CERCA/Generalitat de Catalunya and Fundació Josep Carreras-Obra Social la Caixa for their institutional support. This work was supported by the European Research Council (CoG-2014-646903 to PM), the Spanish Ministry of Economy and Competitiveness (SAF-2016-80481-R to PM), the Asociación Española Contra el Cáncer (AECC-CI-2015), and the ISCIII (PI17/01028) to CB We also acknowledge support from Fundación Leo Messi and the Fundación Uno entre Cienmil. OM was supported by a Lady Tata Memorial Trust (2017) and a "Beatriu de Pinós" postdoctoral fellowship (2018-2019) from Generalitat de Catalunya. DP was supported by an NC3Rs Fellowship and CCLG project grant. The Spanish Ministry of Economy and Competitiveness (SAF-2016-75286-R to RR), The ISC III/FEDER (Miguel Servet Program

CPII16/00049 to RR, Sara Borrell Program CD16/00103 to STM and PI16/00280) and Consorcio CIBERONC(CB16/12/00390). PM is an investigator of the Spanish Cell Therapy network (TERCEL).

CONFLICT OF INTEREST DISCLOSURE: The authors have nothing to disclose.

REFERENCES

1. Pui CH, Mullighan CG, Evans WE, Relling MV. Pediatric acute lymphoblastic leukemia: where are we going and how do we get there? *Blood.* Aug 9 2012;120(6):1165-1174.
2. Greaves MF. Aetiology of acute leukaemia. *Lancet.* Feb 1 1997;349(9048):344-349.
3. Harrison CJ, Moorman AV, Barber KE, et al. Interphase molecular cytogenetic screening for chromosomal abnormalities of prognostic significance in childhood acute lymphoblastic leukaemia: a UK Cancer Cytogenetics Group Study. *British journal of haematology.* May 2005;129(4):520-530.
4. Moorman AV, Richards SM, Martineau M, et al. Outcome heterogeneity in childhood high-hyperdiploid acute lymphoblastic leukemia. *Blood.* Oct 15 2003;102(8):2756-2762.
5. Paulsson K, Johansson B. High hyperdiploid childhood acute lymphoblastic leukemia. *Genes, chromosomes & cancer.* Aug 2009;48(8):637-660.
6. Carroll WL. Safety in numbers: hyperdiploidy and prognosis. *Blood.* Mar 28 2013;121(13):2374-2376.
7. Bateman CM, Alpar D, Ford AM, et al. Evolutionary trajectories of hyperdiploid ALL in monozygotic twins. *Leukemia.* Jan 2015;29(1):58-65.
8. Collaborative study of karyotypes in childhood acute lymphoblastic leukemias. Groupe Francais de Cytogenetique Hematologique. *Leukemia.* Jan 1993;7(1):10-19.
9. Moorman AV, Ensor HM, Richards SM, et al. Prognostic effect of chromosomal abnormalities in childhood B-cell precursor acute lymphoblastic leukaemia: results from the UK Medical Research Council ALL97/99 randomised trial. *The Lancet. Oncology.* May 2010;11(5):429-438.
10. Paulsson K, Forestier E, Andersen MK, et al. High modal number and triple trisomies are highly correlated favorable factors in childhood B-cell precursor high hyperdiploid acute lymphoblastic leukemia treated according to the NOPHO ALL 1992/2000 protocols. *Haematologica.* Sep 2013;98(9):1424-1432.
11. Paulsson K, Lilljebjorn H, Biloglav A, et al. The genomic landscape of high hyperdiploid childhood acute lymphoblastic leukemia. *Nature genetics.* Jun 2015;47(6):672-676.
12. Malinowska-Ozdowy K, Frech C, Schonegger A, et al. KRAS and CREBBP mutations: a relapse-linked malicious liaison in childhood high hyperdiploid acute lymphoblastic leukemia. *Leukemia.* Aug 2015;29(8):1656-1667.
13. Gascoigne KE, Cheeseman IM. Kinetochore assembly: if you build it, they will come. *Current opinion in cell biology.* Feb 2011;23(1):102-108.
14. Gordon DJ, Resio B, Pellman D. Causes and consequences of aneuploidy in cancer. *Nature reviews. Genetics.* Mar 2012;13(3):189-203.
15. Soto M, Raaijmakers JA, Medema RH. Consequences of Genomic Diversification Induced by Segregation Errors. *Trends in genetics : TIG.* Feb 8 2019.
16. Potapova T, Gorbsky GJ. The Consequences of Chromosome Segregation Errors in Mitosis and Meiosis. *Biology.* Feb 8 2017;6(1).

17. Krapf G, Kaindl U, Kilbey A, et al. ETV6/RUNX1 abrogates mitotic checkpoint function and targets its key player MAD2L1. *Oncogene.* Jun 3 2010;29(22):3307-3312.
18. Prieto C, Lopez-Millan B, Roca-Ho H, et al. NG2 antigen is involved in leukemia invasiveness and central nervous system infiltration in MLL-rearranged infant B-ALL. *Leukemia.* Mar 2018;32(3):633-644.
19. Torres EM, Williams BR, Tang YC, Amon A. Thoughts on aneuploidy. *Cold Spring Harbor symposia on quantitative biology.* 2010;75:445-451.
20. Santaguida S, Amon A. Short- and long-term effects of chromosome mis-segregation and aneuploidy. *Nature reviews. Molecular cell biology.* Aug 2015;16(8):473-485.
21. Ohashi A, Ohori M, Iwai K, et al. Aneuploidy generates proteotoxic stress and DNA damage concurrently with p53-mediated post-mitotic apoptosis in SAC-impaired cells. *Nature communications.* Jul 6 2015;6:7668.
22. Lilljebjorn H, Agerstam H, Orsmark-Pietras C, et al. RNA-seq identifies clinically relevant fusion genes in leukemia including a novel MEF2D/CSF1R fusion responsive to imatinib. *Leukemia.* Apr 2014;28(4):977-979.
23. Aburawi HE, Biloglav A, Johansson B, Paulsson K. Cytogenetic and molecular genetic characterization of the 'high hyperdiploid' B-cell precursor acute lymphoblastic leukaemia cell line MHH-CALL-2 reveals a near-haploid origin. *British journal of haematology.* Jul 2011;154(2):275-277.
24. Baudoin NC, Cimini D. A guide to classifying mitotic stages and mitotic defects in fixed cells. *Chromosoma.* Jun 2018;127(2):215-227.
25. Boutter J, Huang Y, Marovca B, et al. Image-based RNA interference screening reveals an individual dependence of acute lymphoblastic leukemia on stromal cysteine support. *Oncotarget.* Nov 30 2014;5(22):11501-11512.
26. Manabe A, Coustan-Smith E, Behm FG, Raimondi SC, Campana D. Bone marrow-derived stromal cells prevent apoptotic cell death in B-lineage acute lymphoblastic leukemia. *Blood.* May 1 1992;79(9):2370-2377.
27. Mihara K, Imai C, Coustan-Smith E, et al. Development and functional characterization of human bone marrow mesenchymal cells immortalized by enforced expression of telomerase. *British journal of haematology.* Mar 2003;120(5):846-849.
28. Pal D, Blair HJ, Elder A, et al. Long-term in vitro maintenance of clonal abundance and leukaemia-initiating potential in acute lymphoblastic leukaemia. *Leukemia.* Aug 2016;30(8):1691-1700.
29. Jaqaman K, King EM, Amaro AC, et al. Kinetochore alignment within the metaphase plate is regulated by centromere stiffness and microtubule depolymerases. *The Journal of cell biology.* Mar 8 2010;188(5):665-679.
30. Hengeveld RCC, Vromans MJM, Vleugel M, Hadders MA, Lens SMA. Inner centromere localization of the CPC maintains centromere cohesion and allows mitotic checkpoint silencing. *Nature communications.* May 31 2017;8:15542.
31. Matsui Y, Nakayama Y, Okamoto M, Fukumoto Y, Yamaguchi N. Enrichment of cell populations in metaphase, anaphase, and telophase by synchronization using nocodazole and blebbistatin: a novel method suitable for examining dynamic changes in proteins during mitotic progression. *European journal of cell biology.* May 2012;91(5):413-419.
32. Lagana A, Dorn JF, De Rop V, Ladouceur AM, Maddox AS, Maddox PS. A small GTPase molecular switch regulates epigenetic centromere maintenance by stabilizing newly incorporated CENP-A. *Nature cell biology.* Dec 2010;12(12):1186-1193.
33. Saitoh N, Goldberg I, Earnshaw WC. The SMC proteins and the coming of age of the chromosome scaffold hypothesis. *BioEssays : news and reviews in molecular, cellular and developmental biology.* Sep 1995;17(9):759-766.

34. Hudson DF, Vagnarelli P, Gassmann R, Earnshaw WC. Condensin is required for nonhistone protein assembly and structural integrity of vertebrate mitotic chromosomes. *Developmental cell.* Aug 2003;5(2):323-336.
35. Gassmann R, Vagnarelli P, Hudson D, Earnshaw WC. Mitotic chromosome formation and the condensin paradox. *Experimental cell research.* May 15 2004;296(1):35-42.
36. Woodward J, Taylor GC, Soares DC, et al. Condensin II mutation causes T-cell lymphoma through tissue-specific genome instability. *Genes & development.* Oct 1 2016;30(19):2173-2186.
37. Bazile F, St-Pierre J, D'Amours D. Three-step model for condensin activation during mitotic chromosome condensation. *Cell cycle.* Aug 15 2010;9(16):3243-3255.
38. Hirano T. The ABCs of SMC proteins: two-armed ATPases for chromosome condensation, cohesion, and repair. *Genes & development.* Feb 15 2002;16(4):399-414.
39. Ribeiro SA, Vagnarelli P, Dong Y, et al. A super-resolution map of the vertebrate kinetochore. *Proceedings of the National Academy of Sciences of the United States of America.* Jun 8 2010;107(23):10484-10489.
40. Molina O, Carmena M, Maudlin IE, Earnshaw WC. PREditOR: a synthetic biology approach to removing heterochromatin from cells. *Chromosome Res.* Dec 2016;24(4):495-509.
41. Fukagawa T, Earnshaw WC. The centromere: chromatin foundation for the kinetochore machinery. *Developmental cell.* Sep 08 2014;30(5):496-508.
42. Earnshaw WC, Migeon BR. Three related centromere proteins are absent from the inactive centromere of a stable isodicentric chromosome. *Chromosoma.* 1985;92(4):290-296.
43. Vafa O, Sullivan KF. Chromatin containing CENP-A and alpha-satellite DNA is a major component of the inner kinetochore plate. *Current biology : CB.* Nov 01 1997;7(11):897-900.
44. Warburton PE, Cooke CA, Bourassa S, et al. Immunolocalization of CENP-A suggests a distinct nucleosome structure at the inner kinetochore plate of active centromeres. *Current biology : CB.* Nov 01 1997;7(11):901-904.
45. Allshire RC, Nimmo ER, Ekwall K, Javerzat JP, Cranston G. Mutations derepressing silent centromeric domains in fission yeast disrupt chromosome segregation. *Genes & development.* Jan 15 1995;9(2):218-233.
46. Ekwall K, Javerzat JP, Lorentz A, Schmidt H, Cranston G, Allshire R. The chromodomain protein Swi6: a key component at fission yeast centromeres. *Science.* Sep 8 1995;269(5229):1429-1431.
47. Bannister AJ, Zegerman P, Partridge JF, et al. Selective recognition of methylated lysine 9 on histone H3 by the HP1 chromo domain. *Nature.* Mar 1 2001;410(6824):120-124.
48. Samoshkin A, Arnaoutov A, Jansen LE, et al. Human condensin function is essential for centromeric chromatin assembly and proper sister kinetochore orientation. *PloS one.* Aug 28 2009;4(8):e6831.
49. Green LC, Kalitsis P, Chang TM, et al. Contrasting roles of condensin I and condensin II in mitotic chromosome formation. *Journal of cell science.* Mar 15 2012;125(Pt 6):1591-1604.
50. Trivedi P, Stukenberg PT. A Centromere-Signaling Network Underlies the Coordination among Mitotic Events. *Trends in biochemical sciences.* Feb 2016;41(2):160-174.
51. Liang C, Zhang Z, Chen Q, et al. A positive feedback mechanism ensures proper assembly of the functional inner centromere during mitosis in human cells. *The Journal of biological chemistry.* Feb 1 2019;294(5):1437-1450.

52. Novais-Cruz M, Alba Abad M, van IWF, et al. Mitotic progression, arrest, exit or death relies on centromere structural integrity, rather than de novo transcription. *eLife.* Aug 6 2018;7.
53. Carmena M, Wheelock M, Funabiki H, Earnshaw WC. The chromosomal passenger complex (CPC): from easy rider to the godfather of mitosis. *Nature reviews. Molecular cell biology.* Dec 2012;13(12):789-803.
54. Listovsky T, Sale JE. Sequestration of CDH1 by MAD2L2 prevents premature APC/C activation prior to anaphase onset. *The Journal of cell biology.* Oct 14 2013;203(1):87-100.
55. Maia AT, van der Velden VH, Harrison CJ, et al. Prenatal origin of hyperdiploid acute lymphoblastic leukemia in identical twins. *Leukemia.* Nov 2003;17(11):2202-2206.
56. Maia AT, Tussiwand R, Cazzaniga G, et al. Identification of preleukemic precursors of hyperdiploid acute lymphoblastic leukemia in cord blood. *Genes, chromosomes & cancer.* May 2004;40(1):38-43.
57. Ravichandran MC, Fink S, Clarke MN, Hofer FC, Campbell CS. Genetic interactions between specific chromosome copy number alterations dictate complex aneuploidy patterns. *Genes & development.* Dec 1 2018;32(23-24):1485-1498.
58. Heerema NA, Raimondi SC, Anderson JR, et al. Specific extra chromosomes occur in a modal number dependent pattern in pediatric acute lymphoblastic leukemia. *Genes, chromosomes & cancer.* Jul 2007;46(7):684-693.
59. Talamo A, Chalandon Y, Marazzi A, Jotterand M. Clonal heterogeneity and chromosomal instability at disease presentation in high hyperdiploid acute lymphoblastic leukemia. *Cancer genetics and cytogenetics.* Dec 2010;203(2):209-214.
60. Talamo A, Marazzi A, Rovo A, et al. High hyperdiploid acute lymphoblastic leukemia in adults shows clonal heterogeneity and chromosomal instability at diagnosis and during the course of the disease. *Annals of hematology.* May 2012;91(5):793-796.
61. Alpar D, Pajor G, Varga P, et al. Sequential and hierarchical chromosomal changes and chromosome instability are distinct features of high hyperdiploid pediatric acute lymphoblastic leukemia. *Pediatric blood & cancer.* Dec 2014;61(12):2208-2214.
62. Yang M, Vesterlund M, Siavelis I, et al. Proteogenomics and Hi-C reveal transcriptional dysregulation in high hyperdiploid childhood acute lymphoblastic leukemia. *Nature communications.* Apr 3 2019;10(1):1519.
63. Greaves M. A causal mechanism for childhood acute lymphoblastic leukaemia. *Nature reviews. Cancer.* Aug 2018;18(8):471-484.

FIGURE LEGENDS:

FIGURE 1: HyperD-ALL cells are low proliferative and show a delay in early mitosis. **(a)** Heat map of the top 50 genes more differentially expressed between HyperD (n=58) and non-HyperD (n=30) B-ALL samples. **(b-c)** Top 20 statistically significant up-regulated **(b)** or down-regulated **(c)** biological pathways identified using GSEA for the genes differentially expressed in HyperD *versus* nonHyperD-ALL patients. Coloured bars represent normalized enrichment scores (NES). p-values are shown. **(d)** 16-day proliferation curves for the indicated cell lines, n=3 independent experiments. **(e)** SubG0/SubG1 apoptotic levels identified by FACS for the indicated cell lines, n=3 independent experiments. **(f)** Cell cycle analysis for the indicated cell lines. *Left,* representative cell cycle FACS analysis. *Right*, frequency of cells in G2/M analysed, n=3 independent experiments. **(g)** Representative DNA-Kinetochore-spindle IF staining (DNA, ACA, tubulin, and pericentrin) identifying the different mitotic phases in B-ALL cell lines. The SAC identifies the transition from early to late mitosis. P: Prophase, PM: Prometaphase, M: Metaphase, A: Anaphase, T: Telophase, CK: Cytokinesis. Scale bar=10 μm. **(h,i)** Mitosis progression in B-ALL cell lines. Progression from early to late mitosis **(h)**, and frequency of cells at the indicated mitotic phases **(i)**, n=4 independent experiments. Graphs represent the mean, and error bars represent the s.e.m. *p<0.05, **p<0.01 (Two-way ANOVA).

FIGURE 2: HyperD-ALL primary blasts show a delay in early mitosis associated with chromosome alignment defects in prometaphase. (a) Schematic depicting the experimental design for *ex vivo* growth of primary B-ALL blasts onto nestin+ hBM-MSCs. **(b)** *Left*, representative images of primary non-HyperD and HyperD-B-ALL *ex vivo* cultures on nestin+ hBM-MSCs at the indicated time-points. *Right*, absolute counts of B-ALL primary blasts at the indicated time-points, n=2. **(c,d)** Frequency of apoptotic (SubG0/SubG1) **(c)** and G2/M **(d)** non-HyperD and HyperD-ALL primary cells from BM samples, n=3 patients of each. **(e)** Schematic

depicting the PDX model used to expand primary B-ALL blasts *in vivo*. **(f)** Representative DNA (blue)-Kinetochore (purple)-spindle (red-green) IF staining identifying the different mitotic phases in PDX-expanded B-ALLs. The SAC identifies the transition from early to late mitosis. **(g)** Mitosis progression of PDX-expanded B-ALL primary cells. *Left*, progression from early to late mitosis. *Right*, frequency of cells at the indicated mitotic phases, n=3 non-HyperD and n=5 HyperD PDX-expanded B-ALLs. **(h)** *Left*, representative images of mitotic cells with non-aligned and aligned chromosomes at the metaphase plate. *Right*, frequency of PDX-expanded B-ALL primary blasts showing chromosome alignment at prometaphase/metaphase, n=4 non-HyperD and n=4 HyperD PDX-expanded B-ALLs. **(i)** Schematic depicting the chromosome biorientation assay. **(j)** Representative images of the DNA-Kinetochore-spindle staining in monastrol/MG132-treated cells with 0 (left), 1 (middle) and >2 (right) misaligned chromosomes. (**k**) Quantification of metaphase cells showing misaligned chromosomes, n=3 non-HyperD and n=3 HyperD PDX-expanded B-ALLs. Graphs represent the mean, and error bars represent the s.e.m. *p<0.05, **p<0.01; ***p<0.0001 (Two-way ANOVA). Scale bars=10 μm.

FIGURE 3: Chromosome segregation defects and non-modal karyotypes in HyperD-ALL blasts. (a) Representative DNA (blue)-Kinetochore (green)-spindle (red) IF staining identifying lagging and bridge chromosomes. Yellow arrowheads depict the indicated chromosome segregation defect. **(b)** Frequency of blebbistatin-treated mitotic PDX-expanded primary blasts with lagging and bridge chromosomes, n=151 mitosis from 3 non-HyperD and 96 mitosis from 3 HyperD-ALLs. **(c)** Comparison of modal karyotypes from 50 metaphases from primary HyperD (n=6) and non-HyperD (n=6) B-ALL samples. **(d)** Frequency of cells showing modal karyotype. **(e,f)** FISH analysis using DNA probes for chromosomes 12 (green) and 21 (red) of 200 interphase nuclei from n=3 non-HyperD and 4 HyperD-ALL primary samples. **(e)** Frequency of cells representing the modal clone *versus* minor clones. **(f)** Representative FISH analysis for a

primary non-HyperD and a HyperD-ALL. Graphs represent the mean and error bars represent the s.e.m. *p<0.05, **p<0.01; ***p<0.0001 (Two-way ANOVA). Scale bars=10 μm.

FIGURE 4: HyperD-ALL blasts show chromosome hypocondensation, loss of centromere stiffness, and defects in the condensin complex. (a) Analysis of spindle abnormalities in B-ALL primary blasts. *Left*, representative DNA-Kinetochore-spindle IF staining of mitotic cells with bipolar, multipolar and disorganized spindles. *Right*, frequency of mitotic cells displaying spindle defects, n=3 non-HyperD-ALLs (n=251 mitosis) and n=3 HyperD-ALLs (n=251 mitosis) PDX-expanded samples. **(b)** Frequency of metaphases with hypocondensed chromosomes in primary B-ALL blasts, n=200 metaphases from 4 Non-HyperD and n=250 metaphases from 5 HyperD-ALLs primary samples. *Left*, representative images of normal and hypocondensed metaphase chromosomes. Insets represent 3x magnifications. **(c)** Chromosome structure of formaldehyde-crosslinked PDX-expanded B-ALL samples. *Left*, representative images of metaphase cells with hypocondensed chromosomes. Anti-ACA staining is shown in green. *Right*, frequency of formaldehyde-crosslinked metaphases showing hypocondensed or hypocondensed with unstructured chromosomes in B-ALL primary samples, n=60 metaphases from 3 non-HyperD and n=57 metaphases from 3 HyperD-ALLs. **(d)** Chromosome arm width using PDX-expanded B-ALL samples from *c*, n=191 chromosomes from 3 non-HyperD and n=143 chromosomes from 3 HyperD-ALLs. **(e)** Representative IF images of metaphase PDX-expanded B-ALL blasts stained with DAPI, anti-SMC2 and anti-ACA. **(f)** Quantification of the SMC2 total volume in metaphase chromosomes from *e*, n=30 metaphases from 3 non-HyperD and 3 HyperD-ALLs. **(g)** Schematic cartoon of the two human condensin complexes. **(h)** WB analysis of the indicated condensin members in whole-cell lysates from PDX-expanded B-ALL samples. **(i)** Quantification of WB bands from *h* normalized to actin. **(j)** Representative HPLC-ESI-MS chromatograms of the indicated peptides for HyperD and non-HyperD PDX-expanded B-ALLs. **(k)** Acetylation levels of

SMC2 peptide SQAASILTK (m/z=480.8). **(l)** Phosphorylation levels of CAPD2 peptide GPAASTQEK (m/z=524.7). Results depict the average of the peak areas from independent MS experiments from 2 non-HyperD and 2 HyperD-ALL PDX-expanded blasts. **(m)** Representative line-scan measurements of individual centromeres in the indicated B-ALL primary samples. DAPI and ACA are depicted as a blue and red lines, respectively. Yellow arrowheads point to the analysed chromosome. **(n)** Intercentromeric distance from MG132-treated PDX-expanded B-ALL blasts, n=155 centromeres from 3 non-HyperD and n=119 centromeres from 3 HyperD-ALLs. **(o)** Intercentromeric distance from colcemid-treated PDX-expanded B-ALL blasts, n=130 centromeres from 3 non-HyperD and n=111 centromeres from 3 HyperD-ALLs. Graphs represent the mean and error bars represent the s.em. *p<0.05, **p<0.01; ***p<0.001; **** p<0.0001. Two-way ANOVA (*b,c*) or t-Student (*a,d,f,h,i*). Scale bars=10 μm.

FIGURE 5: Mis-localized AURKB and Survivin from the inner centromere and loss of chromatid cohesion and SAC impairment in HyperD-ALL blasts. (a,b) Representative IF staining for CENP-A and AURKB **(a)** or Survivin **(b)** in PDX-expanded B-ALL blasts. **(c,d)** Quantification of the AURKB **(c)** and Survivin **(d)** fluorescence signal at the inner centromere, n=30 metaphases from 3 non-HyperD and n=30 metaphases from 3 HyperD-ALL. **(e)** Representative IF showing either centromeric and scattered localization of AURKB, Survivin and CENP-A. **(f,g)** Frequency of PDX-expanded non-HyperD (n=3) and HyperD-ALL (n=3) blasts showing centromeric *versus* scattered localization of AURKB (n=797 chromosomes from non-HyperD and n=676 chromosomes from HyperD) **(f)**, and Survivin (n=964 chromosomes from non-HyperD and n=814 chromosomes from HyperD) **(g)**. **(h)** Quantification of total AURKB fluorescence signal from samples in *c*. AURKB levels are expressed relative to non-HyperD blasts, which are arbitrarily set to 100. **(i)** *Left*, representative FACS staining of H3S10P. *Right,* MFI of H3S10P in 3 non-HyperD and 3 HyperD-ALL samples. **(j)** *Left,* representative images of

normal or rail-road shaped chromosomes. *Right,* frequency of metaphases showing the indicated number of chromosomes with PCS; n=200 metaphases from 4 non-HyperD, n=250 metaphases from 5 HyperD-ALLs samples. **(k)** Schematic depicting the workflow for functional analysis of the SAC. **(l)** Representative FACS of mitotic PDX-expanded B-ALL blasts (H3S10P+CD19+ cells, green) in the presence or absence of nocodazole. **(m)** Fold-change of mitotic (H3S10P+) blasts in nocodazol-treated (relative to DMSO-treated) non-HyperD (n=3) and HyperD-ALL (n=3) primary blasts. **(n)** Representative FACS cell cycle distribution of nocodazol- *versus* DMSO-treated PDX-expanded B-ALL blasts. **(o)** Quantification of the cell cycle phases in nocodazol- *versus* DMSO-treated PDX-expanded B-ALL blasts, n=3 non-HyperD and n=3 HyperD-ALL. **(p)** qRT-PCR analysis of SAC proteins in B-ALL primary samples, n=9 non-HyperD and n=11 HyperD. Graphs represent the mean and error bars represent the s.e.m. *p<0.05, **p<0.01; ***p<0.001; **** p<0.0001 (two-way ANOVA or t-Student). Scale bars=10 µm.

FIGURE 6: Inhibition of AURKB and SAC in CD34+ HSPCs reproduces chromosome structure defects and hyperdiploid karyotypes. **(a)** Schematic depicting the workflow for AURKB and SAC inhibition in CD34+ HSPCs. **(b)** Representative images of metaphase chromosomes treated as indicated. **(c-f)** Frequency of metaphases with micronuclei (n=500 cells per experiment) **(c)**, hypocondensed chromosomes **(d)**, PCS **(e)** and hyperdiploidy karyotype **(f)**. **(g)** Representative FACS analysis showing PI staining profiles in CD34+ HSPCs treated as indicated. n=150 metaphases were analysed per treatment from 3 independent experiments. *p<0.05, **p<0.01 (One-tail t-Student).

FIGURE 7: Proposed model of the cellular mechanisms underlying the mitotic and chromosome defects contributing to the pathophysiology of pediatric HyperD-ALL.

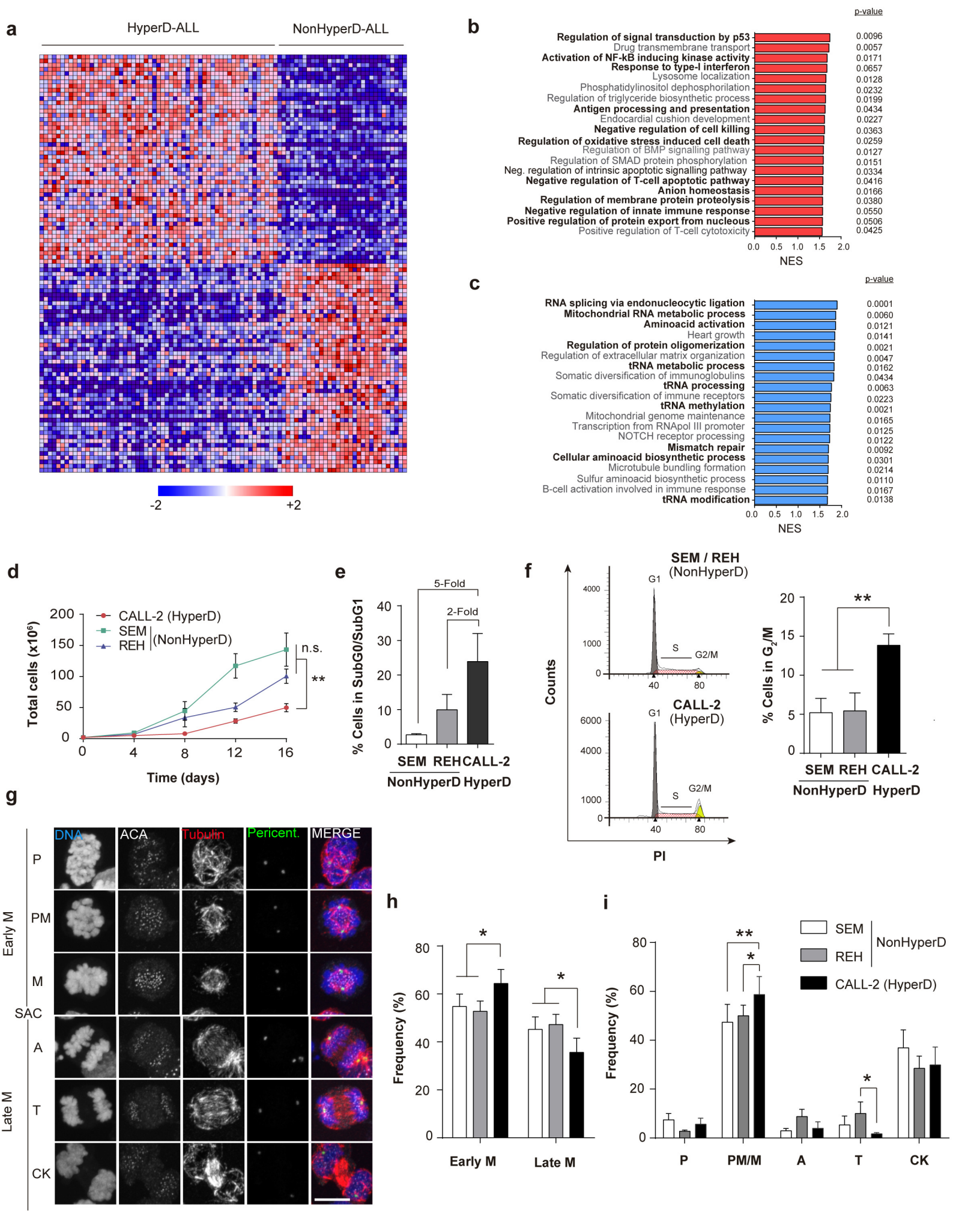

Molina et al. FIGURE 1

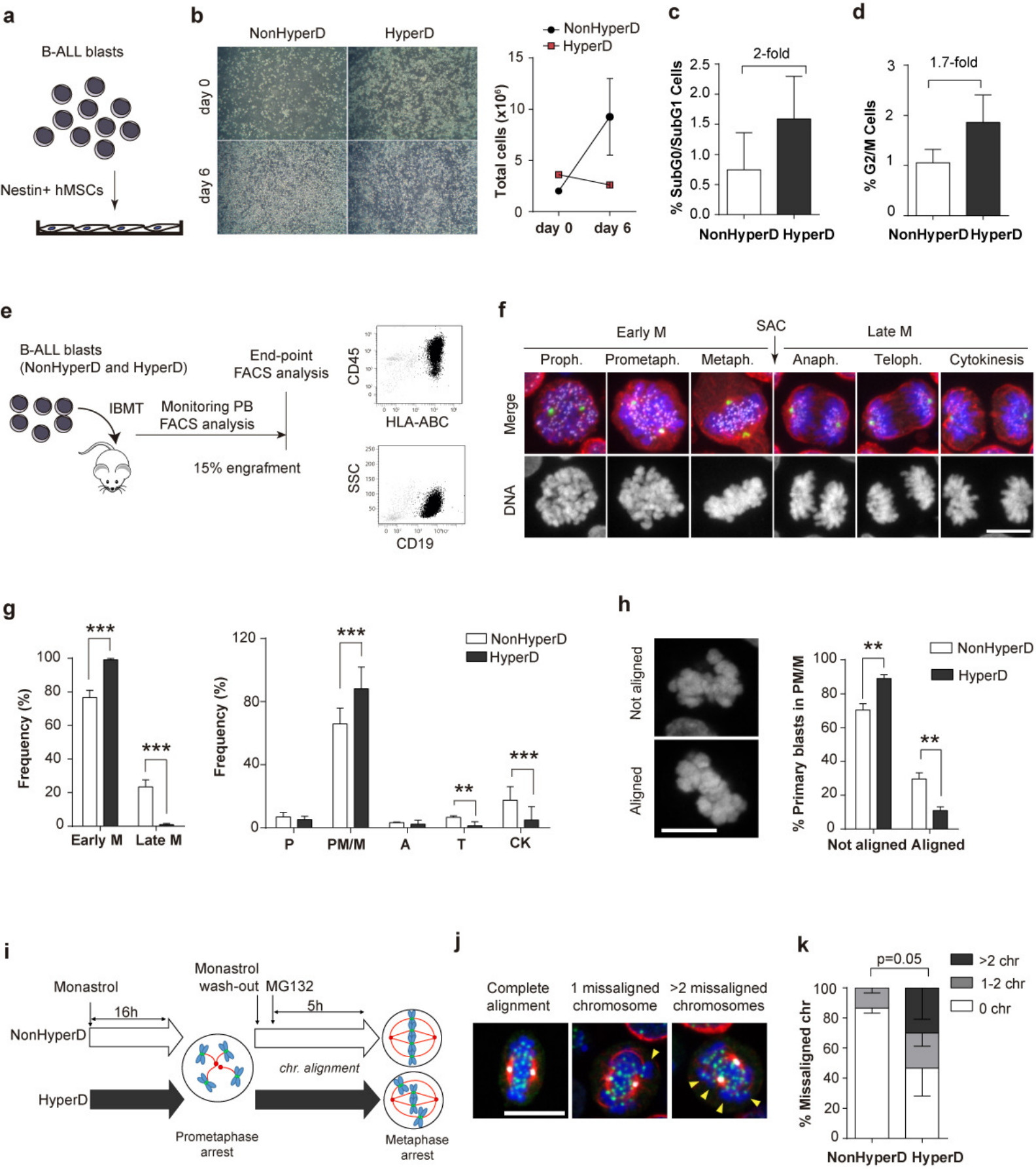

Molina et al. FIGURE 2

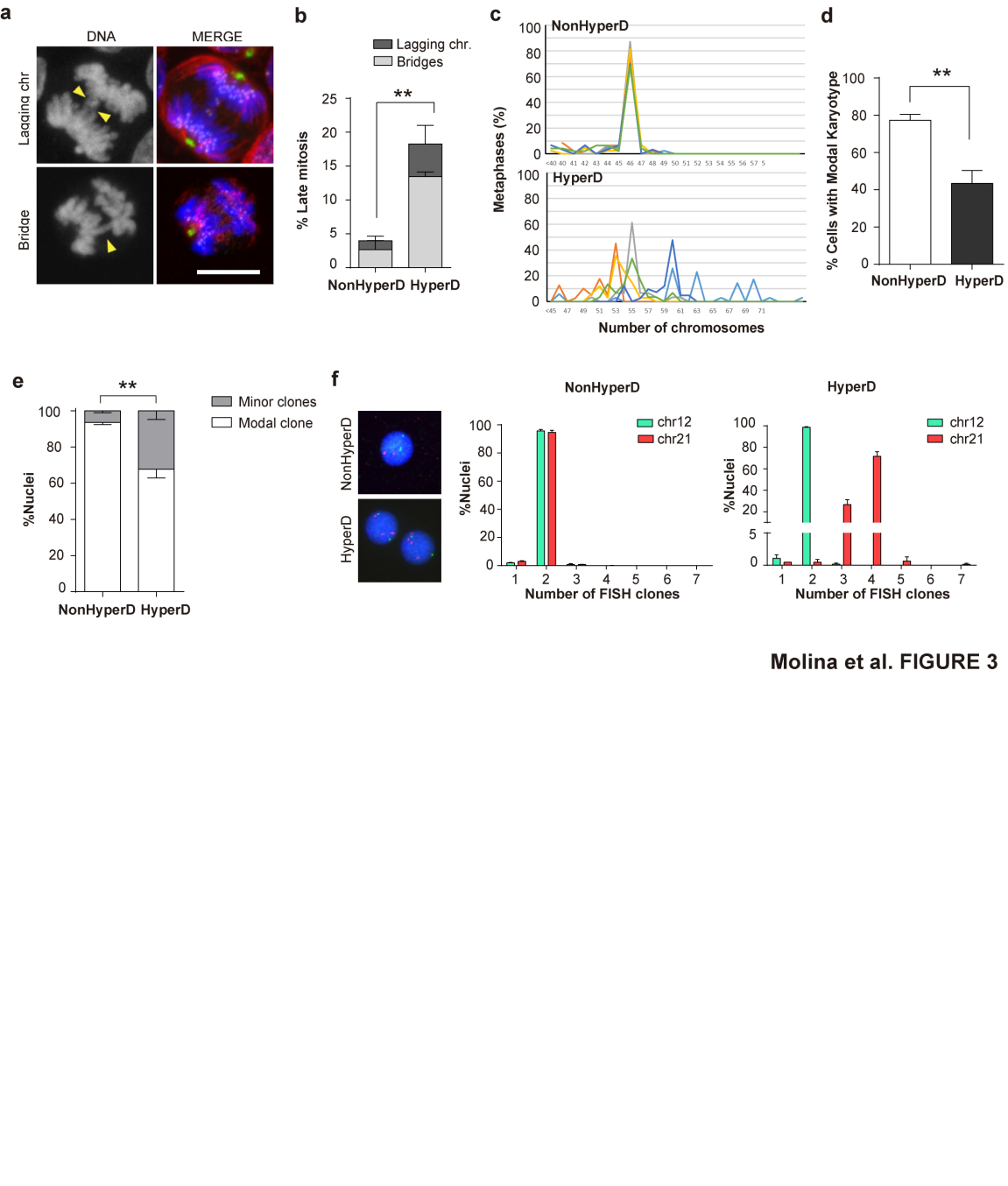

Molina et al. FIGURE 3

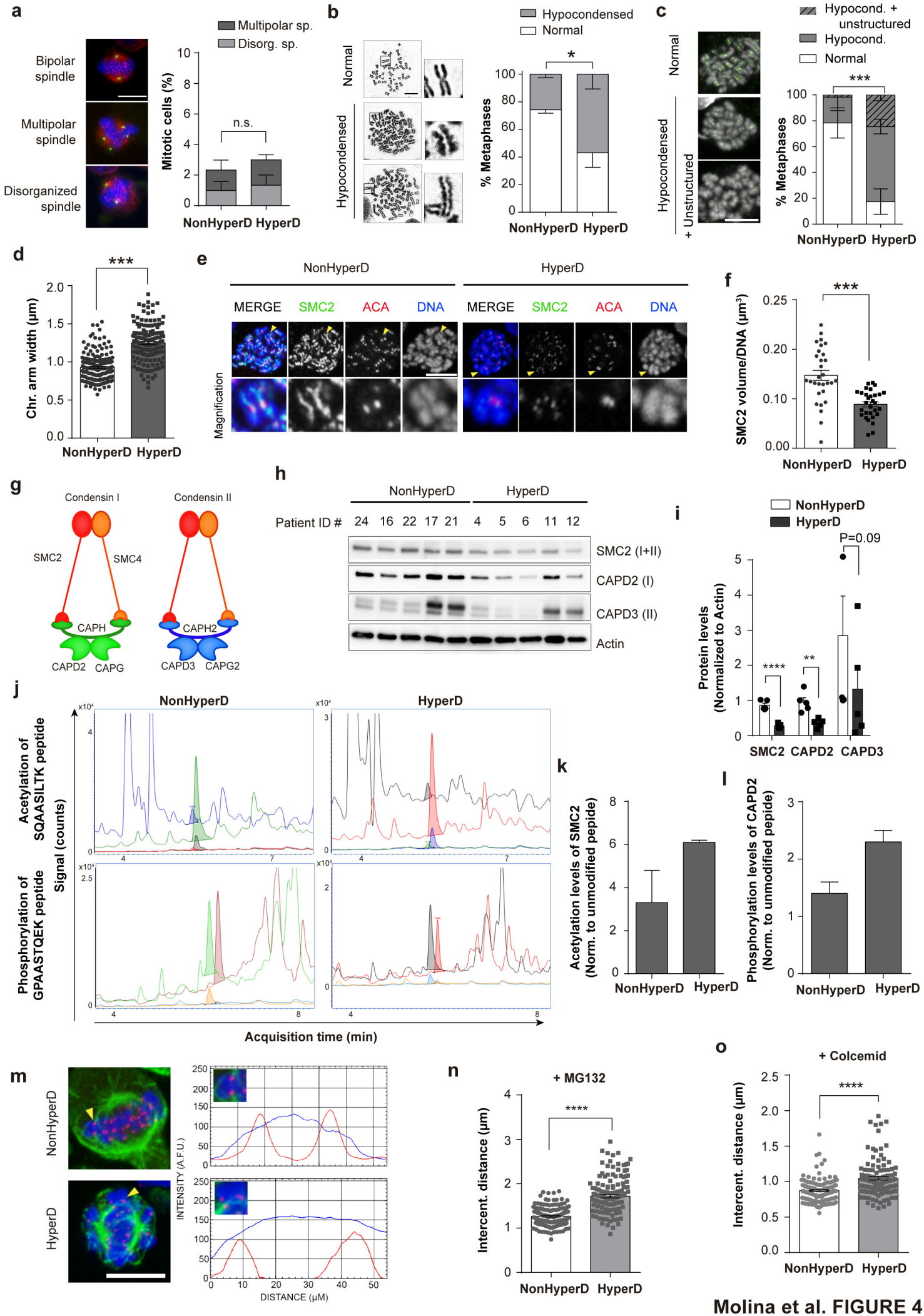

Molina et al. FIGURE 4

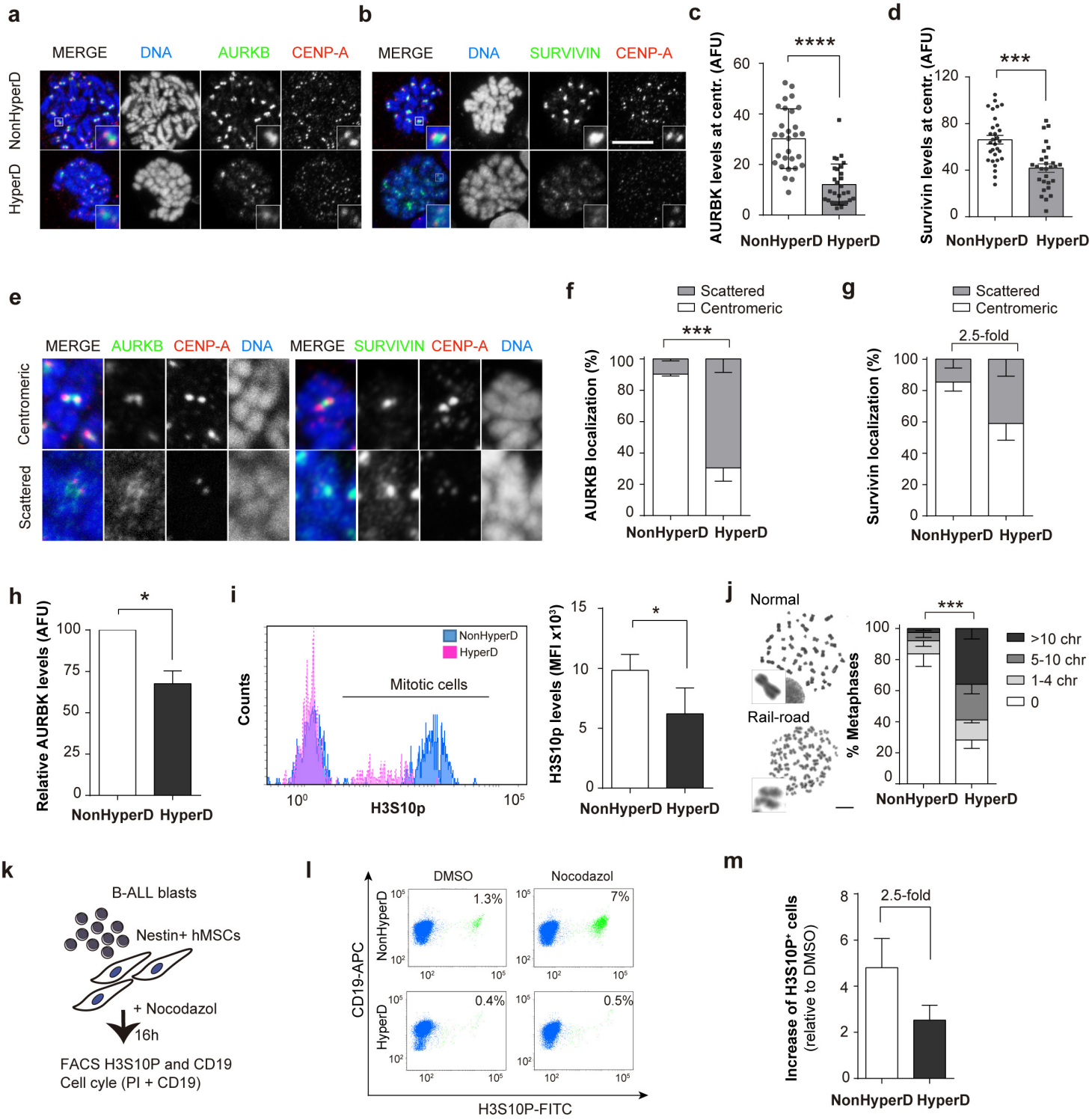

Molina et al. FIGURE 5

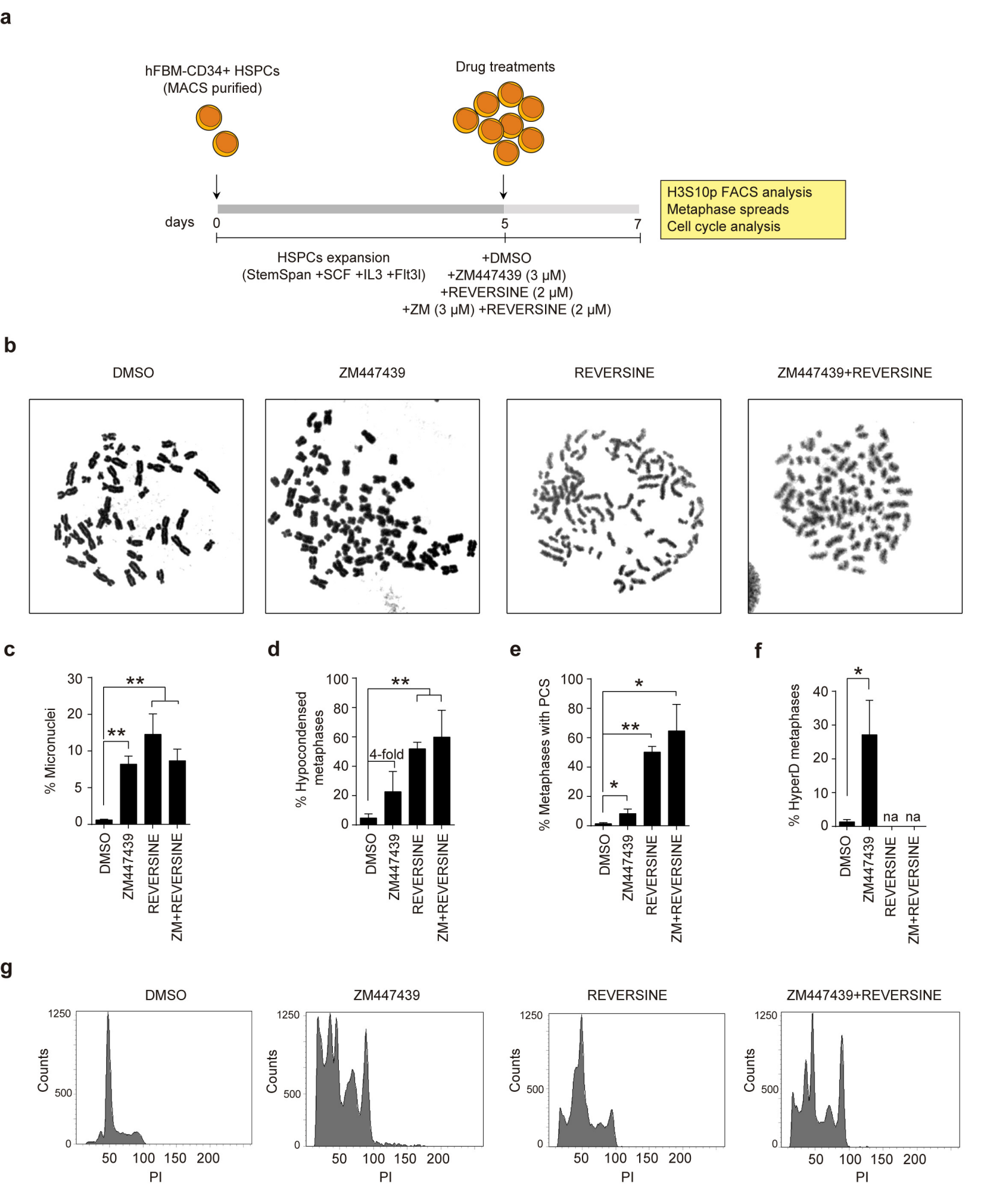

Molina et al. FIGURE 6

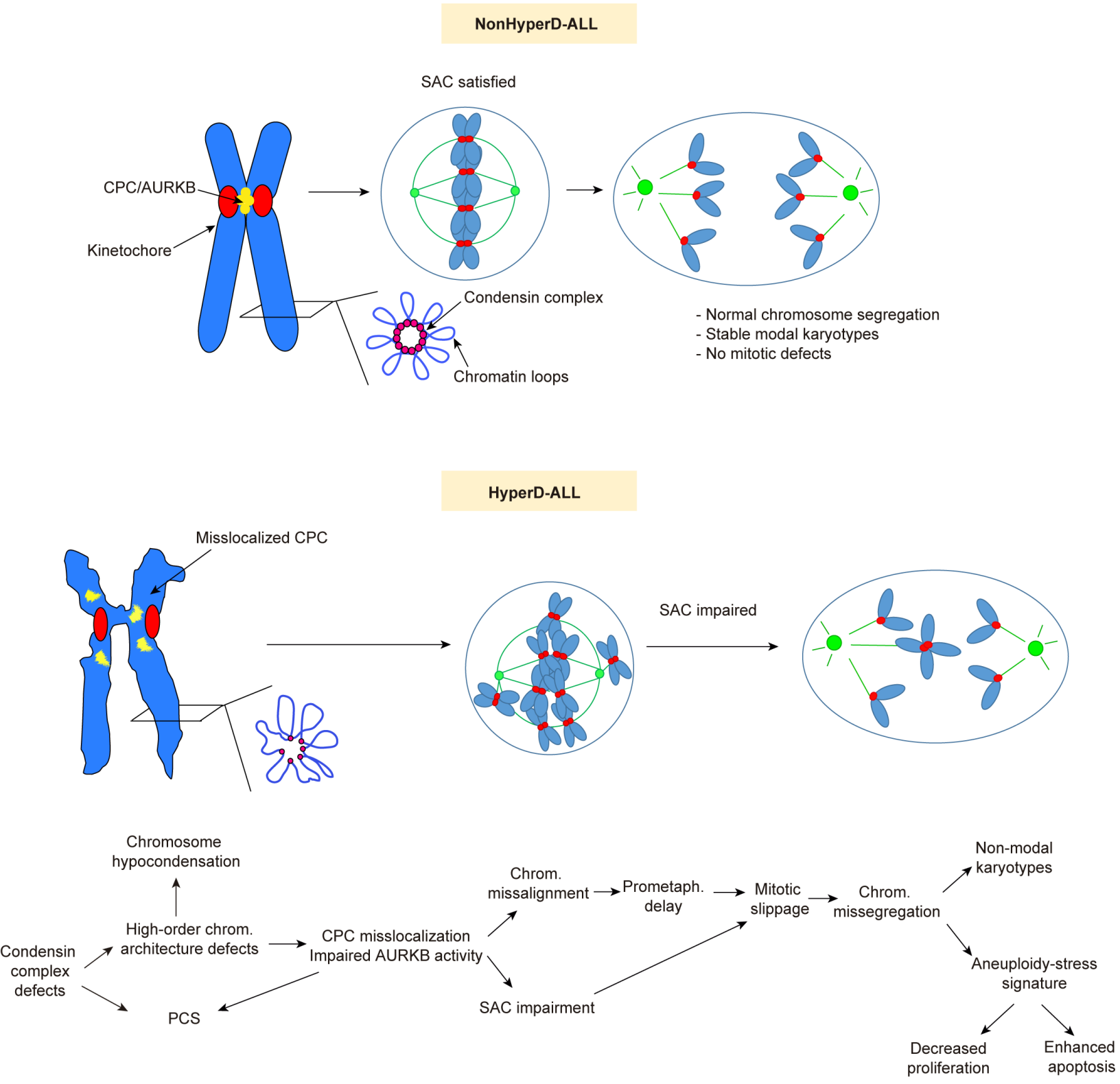

Molina et al. FIGURE 7